J|A|C|S
ARTICLES
Published on Web 07/31/2004

Photoluminescent Layered Lanthanide Silicates

Duarte Ananias,[†] Mariya Kostova,[†] Filipe A. Almeida Paz,[||] Artur Ferreira,[‡] Luís D. Carlos,[§] Jacek Klinowski,[||] and João Rocha*,[†]

Contribution from the Department of Chemistry, CICECO, University of Aveiro, 3810-193 Aveiro, Portugal, ESTGA, CICECO, University of Aveiro, 3810-193 Aveiro, Portugal, Department of Physics, CICECO, University of Aveiro, 3810-193 Aveiro, Portugal, and Department of Chemistry, University of Cambridge, Lensfield Road, Cambridge CB2 1EW, U.K.

Received April 12, 2004; E-mail: rocha@dq.ua.pt

Abstract: The hydrothermal synthesis and structural characterization of layered lanthanide silicates, $K_3[M_{1-a}Ln_aSi_3O_8(OH)_2]$ ($M = Y^{3+}$, Tb^{3+}; $Ln = Eu^{3+}$, Er^{3+}, Tb^{3+}, and Gd^{3+}), named AV-22 materials, are reported. The structure of these solids was elucidated by single-crystal (180 K) and powder X-ray diffraction and further characterized by chemical analysis, thermogravimetry, scanning electron microscopy, ^{29}Si MAS NMR, and photoluminescence spectroscopy. The Er-AV-22 material is a room-temperature infrared phosphor, while Tb- and Eu-AV-22 are visible emitters with output efficiencies comparable to standards used in commercial lamps. The structure of these materials allows the inclusion of a second (or even a third) type of Ln^{3+} ion in the framework and, therefore, the fine-tuning of their photoluminescent properties. For the mixed Tb^{3+}/Eu^{3+} materials, evidence has been found of the inclusion of Eu^{3+} ions in the interlayer space by replacing K^+ ions, further allowing the activation of Tb^{3+}-to-Eu^{3+} energy transfer mechanisms. The occurrence probability of such mechanisms ranges from 0.62 ($a = 0.05$) to 1.20 ms^{-1} ($a = 0.1$) with a high energy transfer efficiency (0.73 and 0.84, respectively).

Introduction

Host−guest chemistry provides a wealth of opportunities for engineering new types of functional materials with tunable properties. In this context, some of our previous work focused on the chemistry of novel zeo-type materials, known as mixed tetrahedral−octahedral microporous silicates, encompassing transition metals such as Ti, Zr, V, and Nb,[1] and more recently the lanthanide elements.[2−4] While research into zeolites made photoluminescent by lanthanide doping (ion exchange) is not new, the preparation of zeolite-type stoichiometric lanthanide silicates is an emerging field.[5] Although, in principle, stoichiometric layered silicates may also exhibit tunable photoluminescence, to the best of our knowledge, there are no comprehensive studies exploring this possibility. While layered coordination polymers have been extensively studied (see, e.g., refs 6 and 7), and some examples of three-dimensional phosphonates consisting of inorganic layers connected by organic groups (reminiscent of pillared structures) are known,[8] the crystal chemistry of layered lanthanide silicates has not yet received the attention it deserves considering (among others) the potential photoluminescent applications of these systems.

Here, we wish to report some of our current work exploring the chemistry of layered lanthanide (Ln^{3+}) silicates and show that, indeed, these are extremely promising tunable photoluminescent systems that may find applications in new types of sensors. In layered silicates, Ln^{3+} ions may be introduced in the sheets or in the interlayer space where, sometimes, it is also possible to intercalate molecules with optical centers. Building on previous structural work on layered $K_3[(Ln)Si_3O_8(OH)_2]$ ($Ln = Ho^{3+}$, Y^{3+}, and Yb^{3+}),[9−11] we have prepared a range of room-temperature photoluminescent solids in the system $K_3[M_{1-a}Ln_aSi_3O_8(OH)_2]$ ($M = Y^{3+}$ and Tb^{3+}; $Ln = Eu^{3+}$, Er^{3+}, Tb^{3+}, and Gd^{3+}). These materials, named AV-22, exhibit remarkable photoluminescence properties which may be tuned by carefully choosing the Ln^{3+} ions and the occupancy of the layer and interlayer metal sites. The hydrothermal syntheses were performed under mild temperature and (autogenous) pressure conditions, contrasting with previous work where 500 °C and 1000−1500 atm were routinely used.

Experimental Section

Syntheses. The syntheses of lamellar silicates were carried out in Teflon-lined autoclaves (volume 37 cm^3, filling rate 0.62), under static

[†] Department of Chemistry, University of Aveiro.
[‡] ESTGA, University of Aveiro.
[§] Department of Physics, University of Aveiro.
[||] Department of Chemistry, University of Cambridge.

(1) Rocha, J.; Anderson, M. W. *Eur. J. Inorg. Chem.* **2000**, 801−818.
(2) Ananias, D.; Ferreira, A.; Rocha, J.; Ferreira, P.; Rainho, J. P.; Morais, C.; Carlos, L. D. *J. Am. Chem. Soc.* **2001**, *123*, 5735−5742.
(3) Ferreira, A.; Ananias, D.; Carlos, D.; Morais, C. M.; Rocha, J. *J. Am. Chem. Soc.* **2003**, *125*, 14573−14579.
(4) Rainho, J.; Carlos, L.; Rocha, J. *J. Lumin.* **2000**, *87*−*89*, 1083−1086.
(5) Rocha, J.; Carlos, L. D. *Curr. Opin. Solid State Mater. Sci.* **2003**, *7*, 199−205.
(6) Pan, L.; Huang, X.; Li, J.; Wu, Y.; Zheng, N. *Angew. Chem., Int. Ed.* **2000**, *39*, 527−530.
(7) Huang, Z.; Strobele, M.; Zhang, K. L.; Meyer, H. J.; You, X. Z.; Yu, Z. *Inorg. Chem. Commun.* **2002**, *5*, 230−234.
(8) Serpaggi, F.; Férey, G. *Inorg. Chem.* **1999**, *38*, 4741−4744.
(9) Ponomarev, V. I.; Filipenko, O. S.; Atovmian, L. O. *Sov. Phys. Dokl.* **1988**, *33*, 87.
(10) Filipenko, O. S.; Shilov, G. V.; Leonova, L. S.; Tkacheva, N: S.; Dimitrova, O. V.; Ponomarev, V. I. *Russ. J. Coord. Chem.* **1999**, *25*, 877−884.
(11) Maksimov, B. A.; Ilyukhin, V. V.; Belov, N. V. *Sov. Phys. Dokl.* **1969**, *13*, 638.

10.1021/ja047905n CCC: $27.50 **© 2004 American Chemical Society**

hydrothermal conditions, in ovens preheated at 230 °C. In all the syntheses, the autoclaves were removed and quenched in cold water after an appropriate time. The obtained microcrystalline powders were filtered, washed at room temperature with distilled water, and dried at 100 °C. Crystals suitable for single-crystal X-ray diffraction could be obtained only in the cases of $K_3[TbSi_3O_8(OH)_2]$ and $K_3[Tb_{0.9}Eu_{0.1}Si_3O_8(OH)_2]$.

A. Typical $K_3YSi_3O_8(OH)_2$, $K_3ErSi_3O_8(OH)_2$, and $K_3EuSi_3O_8(OH)_2$ Synthesis. An alkaline solution was made by mixing 4.45 g of sodium silicate solution (27% m/m SiO_2, 8% m/m Na_2O; Merck), 15.97 g of H_2O, and 7.69 g of KOH (Merck). An amount of 1.69 g of $YCl_3 \cdot 6H_2O$ (Aldrich) was added to this solution, and the mixture was stirred thoroughly. The gel, with composition $0.28Na_2O$:3.42 K_2O:1.0 SiO_2:$0.14Y_2O_3$:$44H_2O$, was autoclaved under autogenous pressure for 7 days at 230 °C. Er and Eu lamellar silicates were synthesized with substitution of $YCl_3 \cdot 6H_2O$ by $LnCl_3 \cdot 6H_2O$, Ln = Er^{3+} or Eu^{3+} (Aldrich). $K_3[Y_{1-a}Er_aSi_3O_8(OH)_2]$ (a = 0.005−1) samples were prepared by introducing the desired Er^{3+} and Y^{3+} contents in the initial gel.

B. Typical $K_3TbSi_3O_8(OH)_2$ Synthesis. An alkaline solution was made by mixing 1.24 g of precipitate-SiO_2 (93% m/m SiO_2, Riedel-de Haën), 20.32 g of H_2O, and 9.12 g of KOH (Merck). An amount of 0.82 g of $TbCl_3 \cdot 6H_2O$ (Aldrich) was added to this solution, and the mixture was stirred thoroughly. The gel, with composition $4.23K_2O$:$1.0SiO_2$:$0.06Tb_2O_3$:$58H_2O$ was autoclaved under autogenous pressure for 7 days at 230 °C. $K_3[Y_{1-a}Tb_aSi_3O_8(OH)_2]$ (a = 0.05−1) samples were synthesized by introducing the desired Tb^{3+} and Y^{3+} contents in the initial gel. $K_3[Tb_{1-a}Eu_aSi_3O_8(OH)_2]$ (a = 0.05−0.1) and $K_3[Gd_{0.67}Tb_{0.28}Eu_{0.05}Si_3O_8(OH)_2]$ samples were prepared by introducing the desired Eu^{3+}, Tb^{3+}, and Gd^{3+} contents in the initial gel.

Within experimental error, chemical analysis by energy-dispersive spectrometry (EDS) confirmed the K:Ln:Si molar ratios obtained by powder X-ray diffraction (XRD), ca. 3:1:3. Samples $K_3[Tb_{1-a}Eu_aSi_3O_8(OH)_2]$, $1 \geq a > 0$, contained a small excess of Ln^{3+} ions [(K/Tb + Eu) molar ratio 2.8−2.9]. For mixed Ln^{3+} samples, no crystals rich in an individual lanthanide were found. All results indicated that lanthanides are randomly distributed within the crystals.

TGA revealed a weight loss step at 550−600 °C. The total weight loss between 26 and 700 °C was 3.91, 3.53, 3.45, and 3.33%, respectively, for Y-, Eu-, Tb-, and Er-AV-22 materials, corresponding to ca. 1 water molecule.

Measurements. X-ray diffraction analysis was performed on suitable single crystals of $K_3[TbSi_3O_8(OH)_2]$ and $K_3[Tb_{0.9}Eu_{0.1}Si_3O_8(OH)_2]$. As the two crystal structures were found to be identical [selected crystal data for the latter structure: orthorhombic, *Pnma* space group, with a = 13.212(3) Å, b = 13.544(3) Å, c = 5.9094(12) Å, V = 1057.4(4) Å^3, Z = 4, R1 [$I > 2\sigma(I)$] = 0.0422, and wR2 (all data) = 0.1199], we only report on the former material. Crystals were mounted on a glass fiber using perfluoropolyether oil.[12] Data were collected at 180(2) K on a Nonius Kappa charge coupled device (CCD) area-detector diffractrometer (Mo Kα graphite-monochromated radiation, λ = 0.7107 Å), equipped with an Oxford Cryosystems cryostream and controlled by the Collect software package.[13] Images were processed by Denzo and Scalepack,[14] and the data were corrected for absorption by using the empirical method employed in Sortav.[15] Structures were solved by the direct methods of SHELXS-97,[16] and refined by full-matrix least squares on F^2 using SHELXL-97.[17] All atoms were directly located from difference Fourier maps and refined with anisotropic displacement parameters, except for H(1), which was refined with an isotropic thermal displacement parameter (U_{iso}) fixed at 1.5U_{eq} of the parent atom [O(3)]. The O−H bond distance was also restrained to 0.95(1) Å. This was intended to provide the best hydrogen-bonding fit for the X-ray data, but it does not reflect the true position of the hydrogen nucleus. The last difference Fourier map synthesis for $K_3[TbSi_3O_8(OH)_2]$ showed a residual electron density with the highest peak (1.703 e Å^{-3}) located at 1.38 Å from O(6) and the deepest hole (−1.935 e Å^{-3}) located at 1.01 Å from Tb(1). Table 1 collects information concerning crystallographic data collection and structure refinement of $K_3[TbSi_3O_8(OH)_2]$. Selected bond lengths and angles are given in the Figure 1 caption.

Table 1. Crystal Data and Structure Refinement Information for $K_3[TbSi_3O_8(OH)_2]$

formula	$H_2K_3O_{10}Si_3Tb$
formula weight	522.51
crystal system	orthorhombic
space group	Pnma
a/Å	13.210(3)
b/Å	13.543(3)
c/Å	5.9072(12)
volume/Å^3	1056.8(4)
Z	4
D_c/g cm^{-3}	3.284
μ(Mo Kα)/mm^{-1}	8.254
F(000)	984
crystal size/mm	0.16 × 0.05 × 0.02
crystal type	colorless blocks
θ range	3.76−27.47
index ranges	$-12 \leq h \leq 17$ $-17 \leq k \leq 17$ $-6 \leq l \leq 7$
reflections collected	5329
independent reflections	1257 (R_{int} = 0.0507)
completeness to θ = 27.47°	99.6%
goodness of fit on F^2	1.085
final R indices [$I > 2\sigma(I)$]	R1 = 0.0339 wR2 = 0.0838
final R indices (all data)	R1 = 0.0408 wR2 = 0.0876
largest diff peak and hole	1.703 and −1.935 e Å^{-3}

SEM images were recorded on a Hitachi S-4100 microscope. EDS was carried out using an EDS Römteck System with polymeric window attached to the scanning electron microscope. Thermogravimetric analysis (TGA) curves were measured with a Labsys TG-DTA1600°Crod, from TA Instruments, in an atmosphere of nitrogen. The samples were heated in air at a rate of 10 °C/min.

Powder X-ray diffraction (XRD) data were collected on an X'Pert MPD Philips diffractometer (Cu Kα X-radiation) with a curved graphite monochromator, a fixed divergence slit of 1/4°, and a flat plate sample holder, in a Bragg−Brentano parafocusing optics configuration. Intensity data were collected by the step counting method (step 0.03° and time 55 s) in the range 12°−130° 2θ.

^{29}Si magic angle spinning (MAS) NMR spectra were recorded at 79.49 MHz on a (9.4 T) Bruker Avance 400 spectrometer, using 40° pulses, spinning rates of 5 (Y-AV-22) and 15 kHz (samples containing Ln^{3+} ions), and, respectively, 60 or 1 s recycle delays. For ^{1}H high-power decoupling, the ^{1}H radio frequency field amplitude was 100 kHz. ^{1}H−^{29}Si cross-polarization (CP) MAS NMR spectra were recorded with 8 ms contact time and 1 s recycle delays. Chemical shifts are quoted in parts per million from TMS.

Photoluminescence measurements were recorded on a Fluorolog-3 Model FL3-2T with a double excitation spectrometer (Triax 320), fitted with a 1200 grooves/mm grating blazed at 330 nm, and a single emission spectrometer (Triax 320), fitted with a 1200 grooves/mm

(12) Kottke, T.; Stalke, D. *J. Appl. Crystallogr.* **1993**, *26*, 615−619.
(13) Hooft, R.; Nonius, B. V. Delft, The Netherlands, 1998.
(14) Otwinowski, Z.; Minor, W. *Macromolecular Crystallography, Part A*; Carter, C. W., Jr., Sweet, R. M., Eds.; Methods in Enzymology 276; Academic Press: New York, 1997; pp 307−326.
(15) (a) Blessing, R. H. *Acta Crystallogr., Sect. A* **1995**, *51*, 33−38. (b) Blessing, R. H. *J. Appl. Crystallogr.* **1997**, *30*, 421−426.
(16) Sheldrick, G. M. *SHELXS 97, Program for Crystal Structure Solution*; University of Göttingen, 1997.
(17) Sheldrick, G. M. *SHELXL 97, Program for Crystal Structure Refinement*; University of Göttingen, 1997.

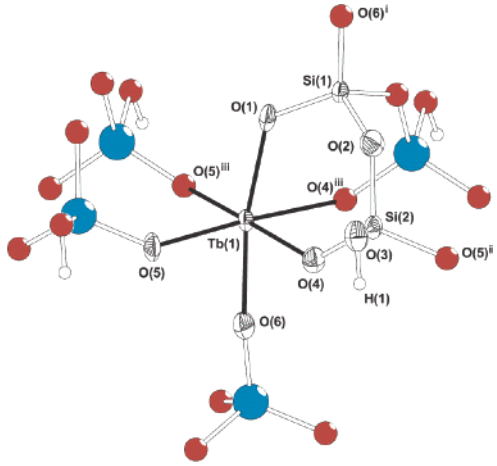

Figure 1. Perspective view of a portion of the $[TbSi_3O_8(OH)_2]^{3-}$ anionic layer of Tb-AV-22. Atoms belonging to the asymmetric unit are represented with thermal displacement ellipsoids drawn at the 80% probability level. H atoms are shown as small spheres. Selected bond lengths (in Å): Tb(1)−O(1) 2.236(5); Tb(1)−O(4) 2.339(4); Tb(1)−O(5) 2.279(4); Tb(1)−O(6) 2.225(6); Si(1)−O(1) 1.594(5); Si(1)−O(2) 1.656(4); Si(1)−O(6)^{i} 1.601(6); Si(2)−O(2) 1.650(4); Si(2)−O(3) 1.669(4); Si(2)−O(4) 1.612(4); Si(2)−O(5)^{ii} 1.600(4). Selected bond angles (in deg): O(1)−Tb(1)−O(4) 83.78(13); O(1)−Tb(1)−O(5) 98.50(12); O(4)−Tb(1)−O(4)^{iii} 88.62(19); O(5)−Tb(1)−O(4) 88.88(15); O(5)−Tb(1)−O(4)^{iii} 176.42(12); O(5)^{iii}−Tb(1)−O(5) 93.5(2); O(6)−Tb(1)−O(1) 169.81(18); O(6)−Tb(1)−O(4) 88.95(12); O(6)−Tb(1)−O(5) 88.44(12). Symmetry codes used to generate equivalent atoms: (i) $x + 1/2, y, 1/2 - z$; (ii) $x, y, z + 1$; (iii) $x, 1/2 - y, z$.

grating blazed at 500 nm, coupled to an R928P photomultiplier. The excitation source was a 450 W xenon lamp. Excitation spectra were corrected from 240 to 600 nm for the spectral distribution of the lamp intensity using a photodiode reference detector. Emission and excitation spectra were also corrected for the spectral response of the monochromators and the detector using typical correction spectra provided by the manufacturer. The time-resolved measurements were carried out using a 1934D3 phosphorimeter coupled to the Fluorolog-3, and a xenon flash lamp (5 mJ/pulse, 3 μs bandwidth) was used as the excitation source. The measurements at 10 K were performed using a He closed-cycle cryostat.

Results and Discussion

Structural Studies. The crystal structure of $K_3[TbSi_3O_8(OH)_2]$ (Tb-AV-22) was determined by single-crystal XRD (Table 1) and was found to be identical to that of the analogous compounds containing Ho^{3+} and Y^{3+} previously reported by Ponomarev et al.[9] and Maksimov et al.,[10] respectively. Phase purity and homogeneity of the bulk sample were further confirmed using powder XRD.

Tb-AV-22 contains a single crystallographically unique Tb^{3+} center, TbO_6, coordinated to six SiO_4 tetrahedra (Figure 1), with a geometry best described as a slightly distorted octahedron [Tb−O bond lengths and angles in the 2.225(6)−2.33(4) Å and 83.78(13)°−176.42(12)° ranges, respectively]. The two crystallographically independent silicon tetrahedra have distinct structural functions: SiO_4H tetrahedra [Si(2)] establish corner-sharing bridges between adjacent TbO_6 octahedra, leading to the formation of one-dimensional arrays running along the c axis direction [Tb(1)···Tb(1)^{i} 5.9072(12) Å; symmetry code (i) $x, y, z + 1$]; SiO_4 units [Si(1)] share corners with two SiO_4H tetrahedra and two TbO_6 octahedra [through O(1) and O(6) atoms; Figure 1], establishing links between adjacent one-dimensional arrays [Tb(1)···Tb(1)^{ii} 6.8872(13) Å; symmetry code (ii) $x - 1/2, y, 1/2 - z$] and leading to the formation of a two-dimensional $[TbSi_3O_8(OH)_2]^{3-}$ anionic perforated plane net perpendicular to the b direction (Figures 1 and 2).

The crystal structure of Tb-AV-22 can be described as the parallel packing in an [ABAB···] fashion along the b axis direction of $[TbSi_3O_8(OH)_2]^{3-}$ anionic layers (two per b axis), which are further interconnected through classical strong O−H···O hydrogen bonds between neighboring Si−OH groups [O(3)−H(1)···O(4)^{iii}: d(D−H) = 0.947(10) Å; d(H···A) = 1.73(2) Å; d(D···A) = 2.666(5) Å; ∠(DHA) = 167(7)°; symmetry code (iii) $-x, 1 - y, 1 - z$] (Figure 2).

Two crystallographically unique charge-balancing K^+ cations are located within the channels of the hydrogen-bonded $[TbSi_3O_8(OH)_2]_n^{3n-}$ anionic framework, with the minimum K(1)···K(2)^{iv} distance being 3.7373(16) Å [symmetry code (iv) $x, y, z + 1$]. K(1) is located within the pores of the $[TbSi_3O_8(OH)_2]^{3-}$ layers (Figure 2) and is surrounded by nine O-atoms with K···O distances 2.638(5)−3.248(4) Å. K(2) occupies instead the interlayer space interacting with eight neighboring O-atoms [K···O distances 2.716(4)−3.293(2) Å]. The minimum Tb(1)···K(1)^{ii} and Tb(1)···K(2)^{v} distances are 3.6752(18) and 3.8261(14) Å, respectively [symmetry code (v) $1/2 - x, 1 - y, -1/2 + z$].

The powder XRD patterns of Er-AV-22 and Eu-AV-22 are similar to the pattern of Tb-AV-22 and were indexed with the PowderX package[18] using the first 24 well-resolved lines. An orthorhombic unit cell with a = 13.5264, b = 13.1564, c = 5.8663 Å for Er-AV-22 and a = 13.5928, b = 13.2292, c = 5.9284 Å for Eu-AV-22 was indicated by the TREOR90 indexing program[19] with high figures of merit, M_{24} = 66 and 69, respectively.

The coordinates of atoms of Tb-AV-22 (single-crystal data) were used as the starting point in the Rietveld refinement of the structures of Er- and Eu-AV-22 samples by the FULLPROF program.[20] The final profile analysis refinement was carried out in the range 12.00°−129.99° 2θ for the occurring 997 "independent" reflections and involved the following: structural parameters—31 fractional atomic coordinates; four isotropic temperature factors; two parameters for the preferred orientation function (March's function); profile parameters—one scale factor, one parameter (h) for the pseudo-Voigt peak shape function, three parameters (U, V, W) to describe the angular dependence of the peak full width at half-maximum (fwhm), three unit cell parameters, two peak asymmetry parameters; global parameters—one zero-point shift, six coefficients of polynomial background. Soft constraints to some of the bond distances were applied. The final conventional R-factors were R_P = 9.04, R_{wp} = 11.7, R_{exp} = 7.05, χ^2 = 2.76, and R_B = 5.74 for Er-AV-22, and R_P = 14.4, R_{wp} = 17.6, R_{exp} = 6.80, χ^2 = 6.70, and R_B = 9.52 for Eu-AV-22. The final profile fit for Er-AV-22 is shown in Figure 3. Final lattice parameters are summarized in Table 2 and compared with related data of similar materials.

The ^{29}Si MAS NMR spectrum of Y-AV-22 (Figure 4) displays two resonances at −75.4 and −85.4 ppm in a 2:1 intensity ratio, in accord with the crystal structure which calls

(18) Dong, C. *J. Appl. Crystallogr.* **1999**, *32*, 838.
(19) Werner, P. E.; Eriksson, L.; Westdahl, M. *J. Appl. Crystallogr.* **1985**, *18*, 367−370.
(20) Rodriguez-Carvajal, J. *FULLPROF, Program for Rietveld Refinement and Pattern Matching Analysis*; Abstracts of the Satellite Meeting on Powder Diffraction of the XVth Congress of the International Union of Crystallography, Toulouse, France, 1990; p 127.

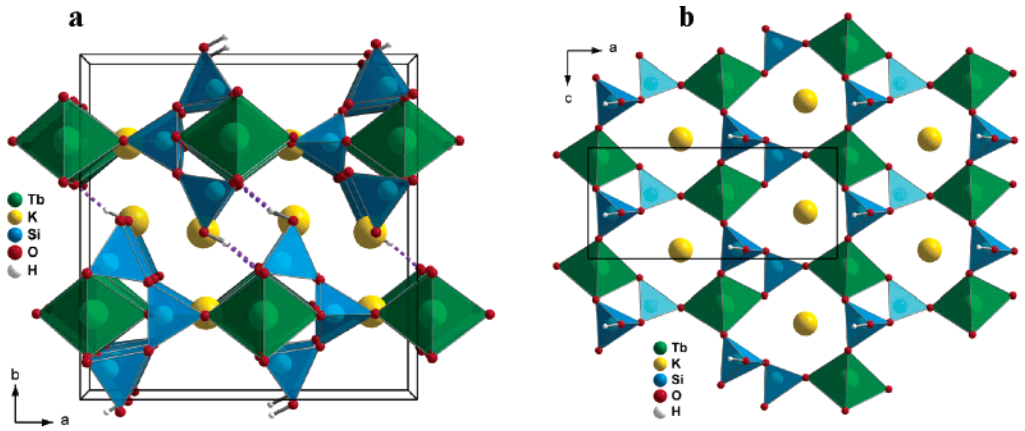

Figure 2. (a) Polyhedral representation of the unit cell contents of Tb-AV-22 viewed along the *c* axis. O−H···O hydrogen bonds are drawn as purple dashed lines and K^+ ions as yellow circles. (b) Perforated, single $[TbSi_3O_8(OH)_2]^{3-}$ layer showing K(1) ions (TbO_6 are depicted in green, SiO_4H and SiO_4 in blue).

Table 2. Unit Cell Parameters of $K_3[MSi_3O_8(OH)_2]$ AV-22 Materials

M	*a* (Å)	*b* (Å)	*c* (Å)	volume (Å^3)	space group
Y[10]	13.536(5)	13.17(1)	5.867(2)	1045.91(9)	Pmnb
Ho[9]	13.534(5)	13.175(5)	5.880(4)	1048.5	Pmnb
Yb[11]	13.088(3)	13.505(3)	5.843(1)	1032.8(4)	Pnma
Eu	13.2462(2)	13.6103(3)	5.9436(2)	1071.54(5)	Pnma
Er	13.1526(3)	13.5228(3)	5.8676(2)	1043.61(5)	Pnma

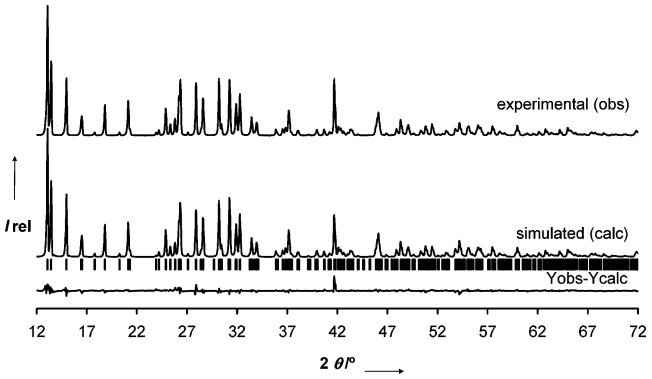

Figure 3. Experimental and simulated powder XRD patterns of Er-AV-22.

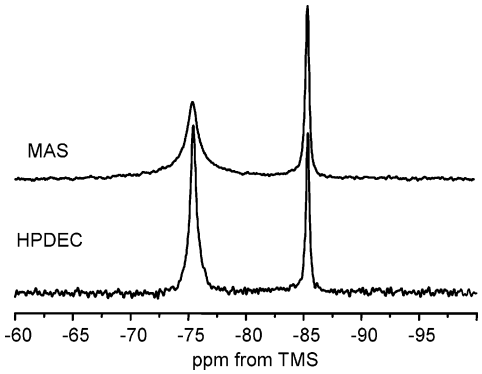

Figure 4. ^{29}Si MAS and high-power ^{1}H decoupling (HPDEC) MAS NMR spectra of $K_3[YSi_3O_8(OH)_2]$ recorded with a 5 kHz spinning rate and 60 s recycle delay.

for the presence of two Si local environments with 2:1 populations. The fwhm of the former peak narrows from 132 to 53 Hz when the spinning rate increases from 5 to 15 kHz. A similar resolution improvement is observed with high-power ^{1}H decoupling at 5 kHz MAS (Figure 4). Moreover, upon ^{1}H−

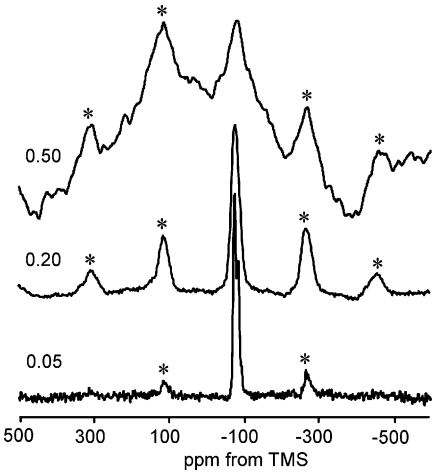

Figure 5. ^{29}Si MAS NMR spectra of $K_3[Y_aEr_{1-a}Si_3O_8(OH)_2]$ (*a* is indicated) recorded with a 15 kHz spinning rate and 60 s recycle delay. Asterisks depict spinning sidebands.

^{29}Si cross-polarization the intensity of the −75.4 ppm peak increases relative to the intensity of the −85.4 ppm resonance. These effects indicate that the −75.4 ppm peak is attributed to ^{29}Si(2), which, being connected to a hydroxyl group, has a significant dipolar interaction with ^{1}H.

The strong paramagnetism of the samples precluded recording acceptable quality ^{29}Si MAS NMR spectra of pure Eu-, Tb-, and Er-AV-22. However, by using fast (15 kHz) MAS rates and short (1 s) recycle delays, we were able to record spectra of some mixed Y^{3+}/Ln^{3+} samples, such as Y-AV-22 with $a = 0.05$ Er, which gives two ^{29}Si MAS NMR peaks in a 2:1 intensity ratio at, respectively, −75.4 and −85.4 ppm (Figure 5). For the $a = 0.20$ Er sample only one resonance is observed at −78.7 ppm, together with several spinning sidebands, while sample $a = 0.50$ Er gives a broad peak at −86.7 ppm and very intense spinning sidebands. No spectra could be recorded at higher Er contents. The broadening of the NMR resonances and

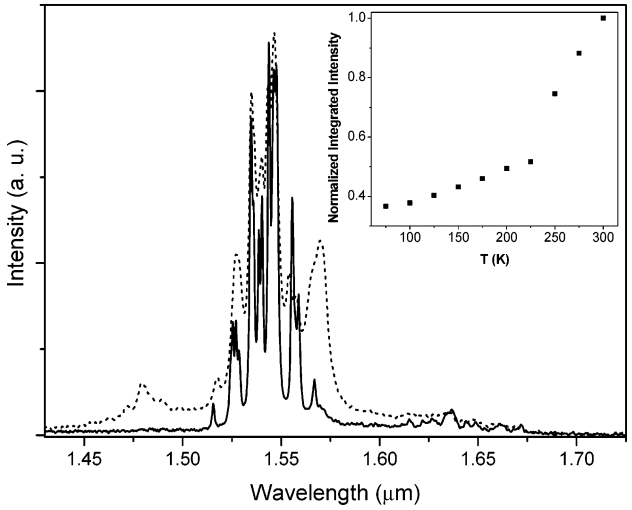

Figure 6. Infrared emission spectra of $K_3[ErSi_3O_8(OH)_2]$ excited at 514.5 nm, recorded at 75 (solid line) and 300 K (dotted line). The inset shows the normalized integrated intensity of the 1.54 μm PL as a function of temperature. The excitation power was 200 mW.

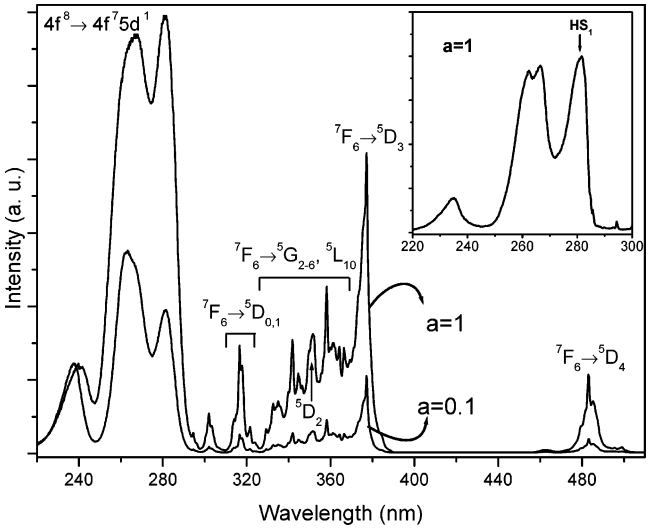

Figure 7. Excitation spectra of $K_3[Y_{1-a}Tb_aSi_3O_8(OH)_2]$ (a = 1, 0.1) recorded monitoring the $^5D_4 \rightarrow {}^7F_5$ transition (540.5 nm) of Tb^{3+} at room temperature. The inset shows the excitation spectrum of a pure Tb^{3+} sample (a = 1) recorded monitoring the $^5D_4 \rightarrow {}^7F_5$ transition at 540.5 nm at 10 K, showing the region in which the transition to the high-spin and low-spin fd states are observed.

the strong spinning sideband patterns observed are caused by the interaction between the Ln^{3+} unpaired electrons and the ^{29}Si nuclei (a through-space dipolar interaction, when the pseudocontact shift is dominant). This clearly shows that Er^{3+} (or other Ln^{3+} ion) is being inserted in the lattice of AV-22, in accord with EDS microanalysis which indicates that (i) the crystallites contain both Y^{3+} and Er^{3+} and (ii) no significant amount of any separated Er^{3+}-rich phase is present.

Photoluminescence Studies. Figure 6 shows the 75 K and room-temperature infrared photoluminescence (PL) spectra of $K_3[ErSi_3O_8(OH)_2]$. The emission lines are assigned to the intra $4f^{11}$ transitions between the $^4I_{13/2}$ and $^4I_{15/2}$ levels of the Er^{3+} ground multiplet. Raising the temperature from 75 to 300 K increases the $^4I_{13/2} \rightarrow {}^4I_{15/2}$ integrated intensity for Er-AV-22 by a factor of ca. 2.7, an effect which is particularly important above ca. 225 K (inset in Figure 6). This is the reverse of the trend usually observed for other siliceous materials, such as Er^{3+}-doped crystalline[21,22] and porous silicon.[23] Recent work on Er^{3+}-doped crystalline silicon reported a similar behavior for 1.54 μm electroluminescence, which was explained in terms of Auger recombinations.[24] For $Na_3ErSi_3O_9$ and Er-AV-9, we have suggested that, as the temperature rises, the redistribution of population between the Stark levels of the fundamental multiplet is probably relevant for understanding this unusual temperature dependence.[25,26]

Figure 7 shows the UV/vis excitation spectra of $K_3[Y_{1-a}Tb_aSi_3O_8(OH)_2]$ for a = 0.1 and 1 (pure Tb^{3+} sample) at room temperature (RT), monitored within the Tb^{3+} $^5D_4 \rightarrow {}^7F_5$ transition (540.5 nm). To allow a quantitative comparison, spectra were consecutively recorded keeping the experimental setup fixed (slit width, irradiated area, optics geometry), and using powders of similar grain size packed in quartz cells. The sharp lines between 300 and 500 nm are assigned to $^7F_6 \rightarrow {}^5D_{4-0}$, $^5L_{10}$, and $^5G_{6-3}$ intraconfigurational forbidden $4f^8 \rightarrow 4f^8$ transitions of Tb^{3+}. The broad band between 250 and 300 nm is ascribed to the spin-forbidden (high-spin, HS) interconfigurational $4f^8 \rightarrow 4f^75d^1$ transition of Tb^{3+}.[27−29] At low temperature (10 K), the HS band distinctly shows three components at ca. 35 510, 37 510, and 38 110 cm^{-1} due to the crystal field splitting of the 5d configuration (inset in Figure 7). This type of spin-forbidden fd band may be observed for (heavy) lanthanide ions with more than seven 4f electrons at an energy lower than the energy of spin-allowed (low-spin, LS) fd transitions.[27,28] The broad band at ca. 234 nm (inset in Figure 7) is assigned to the spin-allowed (LS) interconfigurational fd transition of Tb^{3+}, and the energy separation between the LS and HS fd transitions is ca. 7200 cm^{-1}. This is very similar to the energy separation between the LS and HS fd bands reported for the YPO_4:Tb (1%), CaF_2:Tb (0.1%), and $LiYF_4$:Tb (1%) crystals (7370, 7920, and 7995 cm^{-1}, respectively).[28] We note that the excitation spectra intensity has not been corrected for wavelengths lower than 240 nm and, therefore, the relative intensity of the LS band is not directly comparable.

Figure 8 shows the RT emission spectrum of $K_3[TbSi_3O_8(OH)_2]$ excited at 254 nm, which was selected because it corresponds to the highest excitation line of commercial mercury lamps. The emission lines are assigned to the $^5D_4 \rightarrow {}^7F_J$ (J = 2−6) transitions of Tb^{3+}. Luminescence from the higher (e.g., $^5D_3$) excited states is not detected, even for the samples with the lowest Tb^{3+} content, indicating very efficient nonradiative relaxation to the $^5D_4$ level. The same emission is obtained with excitation either at the maximum of the HS fd band or at the intra $^5D_3$ (377 nm) line. Mixed Y^{3+}/Tb^{3+} samples also display the same emission spectrum. To evaluate the potential use of

(21) Przybylinska, H. H.; Jantsch, W.; Suprun-Belevitch, Y.; Stepikhova, M.; Palmetshofer, L.; Hendorfer, G.; Kozanecki, A.; Wilson, R. J.; Sealy, B. J. *Phys. Rev. B* **1996**, *54*, 2532−2547.
(22) Polman, A. *J. Appl. Phys.* **1997**, *82*, 1−39.
(23) Shin, J. H.; van den Hoven, G. N.; Polman A. *Appl. Phys. Lett.* **1995**, *66*, 2379−2381.
(24) Bresler, M. S.; Gusev, O. B.; Pak, P. E.; Sobolev, N. A.; Yassievich, I. N. *J. Lumin.* **1999**, *80*, 375−379.
(25) Ananias, D.; Rainho, J. P.; Ferreira, A.; Lopes, M.; Morais, C. M.; Rocha, J.; Carlos, L. D. *Chem. Mater.* **2002**, *14*, 1767−1772.
(26) Ananias, D.; Rainho, J. P.; Ferreira, A.; Rocha, J.; Carlos, L. D. *J. Alloys Compd.* **2004**, *374*, 219−222.
(27) Laroche, M.; Doualan, J. L.; Girard, S.; Margerie, J.; Moncorgé, R. *J. Opt. Soc. Am. B* **2000**, *17*, 1291−1303.
(28) van Pierterson, L.; Reid, M. F.; Burdick, G. W.; Meijerink, A. *Phys. Rev. B* **2002**, *65*, 045114.
(29) Hazenkamp, M. F.; Blasse G. *Chem. Mater.* **1990**, *2*, 105−110.

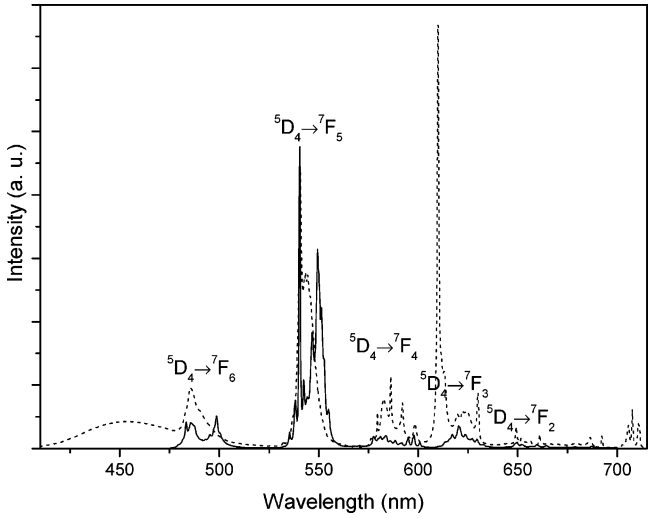

Figure 8. Room-temperature emission spectra of $K_3[TbSi_3O_8(OH)_2]$ (solid line) and a commercial energy-saving 18 W CHINT lamp (dashed line) excited at 254 nm.

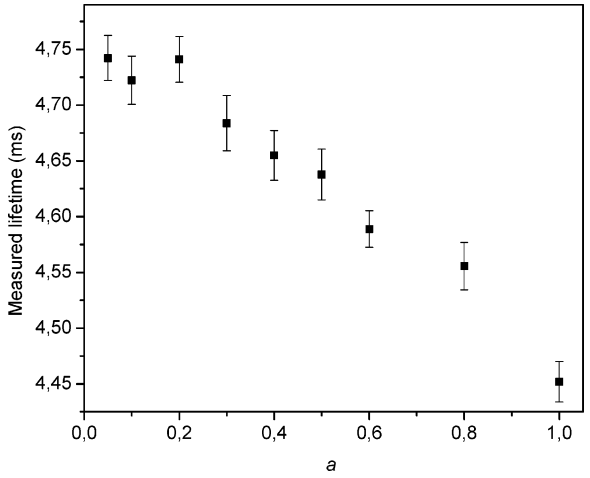

Figure 9. Lifetime of the $^5D_4$ level of Tb^{3+} detected at the strongest $^7F_5$ manifold and excited at 377 nm, as a function of Tb^{3+} content, *a*, in $K_3[Y_{1-a}Tb_aSi_3O_8(OH)_2]$.

this phosphor in commercial energy-saving lamps, the emission efficiency was qualitatively compared to that characteristic of the power of a standard commercial lamp. The standard used is 18 W CHINT,[30] and its emission spectrum is displayed in Figure 8. The two spectra were measured, keeping the experimental setup fixed (slit width, irradiated area, and optics geometry). The two powders have different grain sizes and thus different cross-absorptions. The integrated intensity of the $^5D_4 \rightarrow {}^7F_5$ transition of the pure Tb^{3+} sample is about 0.87 of the integrated intensity of the mixture of lanthanide ions used in the commercial energy-saving lamp.

Figure 9 shows the RT lifetimes for the $^5D_4$ level of Tb^{3+} in $K_3[Y_{1-a}Tb_aSi_3O_8(OH)_2]$. The lifetime curves (not shown) of all samples are well fitted by a single exponential, indicating the presence of a single Tb^{3+} environment, in accord with the crystal structure. Different excitation wavelengths (namely 280 nm, within the $4f\,{}^7 5d^1$) give similar $^5D_4$ lifetime values which remain essentially constant at ca. 4.74 ± 0.02 ms up to $a = 0.2$, when it decreases linearly to ca. 4.45 ± 0.02 ms. Therefore, the $^5D_4$ lifetime only decreases by about 7%, indicating that the energy migration between Tb^{3+} ions is negligible. Nonradiative energy transfer from sensitizers to activators may occur via exchange interaction (requiring orbital overlap) and direct, through-space, multipolar interactions.[31−33]

(30) CHINT is a product of the Chint Group Corporation (http://www.chint.com), PRC.

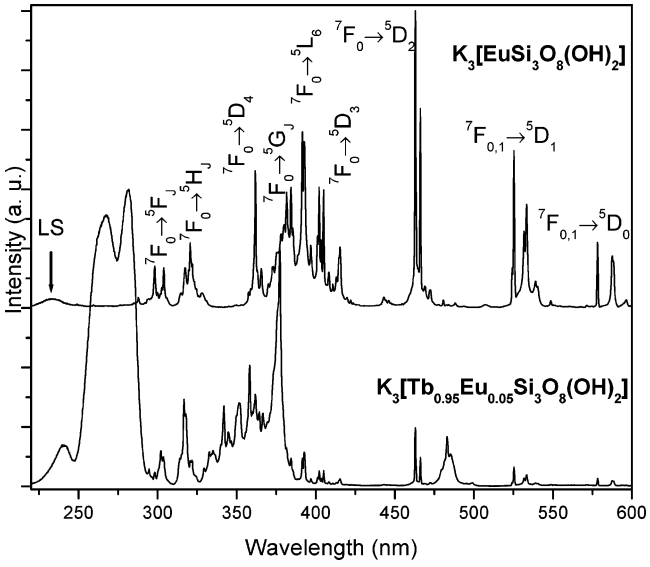

Figure 10. RT excitation spectra of $K_3[EuSi_3O_8(OH)_2]$ and $K_3[Tb_{0.95}Eu_{0.05}Si_3O_8(OH)_2]$, monitored at the $^5D_0 \rightarrow {}^7F_2$ (610.5 nm) transition.

Because in AV-22 the TbO_6 octahedra are isolated from each other by six SiO_4 tetrahedra and the shortest Tb−Tb distance is almost 6.9 Å, a direct overlap of orbitals on different Tb^{3+} ions is difficult and, thus, the occurrence of exchange interaction mechanisms is unlikely.[31,32] Furthermore, the relatively small concentration quenching effect observed indicates that multipolar interactions between Tb^{3+} ions are unlikely.

Assuming that only nonradiative and radiative processes are essentially involved in the depopulation of the $^5D_4$ state, the efficiency, *q*, may be defined as $q = \tau_{exp}/\tau_r$, where the experimental lifetime (τ_{exp}) is directly related to the radiative (k_r) and nonradiative (k_{nr}) probabilities of Tb^{3+}, $\tau_{exp} = (k_r + k_{nr})^{-1}$; τ_r is the inverse of the radiative probability (lifetime in the absence of quenching). Taking τ_r as the lifetime at 10 K (5.15 ± 0.02 ms) of $a = 0.05$ sample (no measurable quenching concentration) and considering the RT lifetime (4.78 ± 0.02 ms), the efficiency of the $^5D_4 \rightarrow {}^7F_5$ emission is estimated to be 0.92.

The excitation spectrum of $K_3[EuSi_3O_8(OH)_2]$ monitored within the Eu^{3+} $^5D_0 \rightarrow {}^7F_2$ (610.5 nm) transition (Figure 10) displays a series of sharp lines assigned to the $^7F_{0-1} \rightarrow {}^5D_{4-0}$, $^5L_6$, ^5G_J ($J = 2-6$), ^5H_J ($J = 3-7$), and ^5F_J ($J = 1-5$) Eu^{3+} intra $4f^6 \rightarrow 4f^6$ transitions. The faint broad (LS) band at high energy is probably the beginning of the spin-allowed, interconfigurational fd, Eu^{3+} transition band, which normally appears at an energy higher than the equivalent Tb^{3+} band.

The RT emission spectra of $K_3[EuSi_3O_8(OH)_2]$ (excited at 394 nm) is shown in Figure 11. The sharp emission lines are assigned to transitions between the first excited nondegenerate

(31) Ke, H.-Y. D.; Birnbaum R. *J. Lumin.* **1995**, *63*, 9−17.
(32) You, H. P.; Wu, X. Y.; Cui, H. T.; Hong G. Y. *J. Lumin.* **2003**, *104*, 223−227.
(33) Reisfeld, R.; Jørgenson, C. K. *Handbook on the Physics and Chemistry of Rare Earths*; Gschneider, K. A., Jr., Eyring, L., Eds.; Elsevier Science Publishers: Amsterdam, 1987; Vol. 9, p 61.

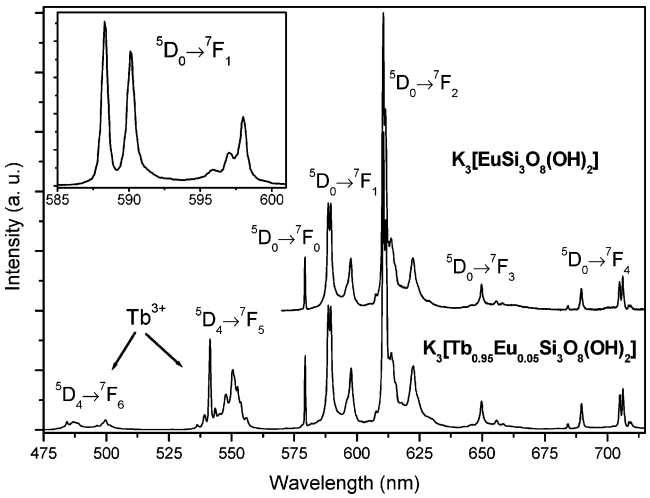

Figure 11. RT emission spectra of $K_3[EuSi_3O_8(OH)_2]$ and $K_3[Tb_{0.95}Eu_{0.05}Si_3O_8(OH)_2]$ excited at 394 ($^5L_6$ Eu^{3+} level) and 377 nm ($^5D_3$ Tb^{3+} level), respectively. The inset shows an expansion of the Eu^{3+} $^5D_0 \rightarrow ^7F_1$ transition collected at 10 K for the pure Eu^{3+} sample.

$^5D_0$ state and the $^7F_{0-4}$ levels of the fundamental Eu^{3+} septet. Eu^{3+} luminescence from higher excited states, such as $^5D_1$, is not detected, indicating very efficient nonradiative relaxation to the $^5D_0$ level. The local-field splitting of the $^5D_0 \rightarrow ^7F_1$ transition in five Stark components (inset in Figure 11) clearly shows the presence of two distinct Eu^{3+} environments. According to the XRD structure, both the Eu^{3+} ions residing in the layers and the K(1) ions (on the plane of the layers) are located on a mirror plane of the *Pnma* (D_{2h}^{16}) space group, whereas K(2) ions in the interlayer space are in a general crystallographic position (Figure 2). Thus, since the group-theoretical selection rules of the D_{2h} space group do not allow the occurrence of $^5D_0 \rightarrow ^7F_0$ line and $^5D_0 \rightarrow ^7F_2$ electric-dipole transitions with intensities greater than the $^5D_0 \rightarrow ^7F_1$ magnetic-dipole lines,[34] some Eu^{3+} ions must inevitably occupy the K(2) positions. This is supported by EDS chemical analysis which revealed a K/Eu molar ratio of ca. 2.9 slightly smaller than 3.

Lifetime measurements (Figure 12) confirm the presence of two local Eu^{3+} environments in $K_3[EuSi_3O_8(OH)_2]$. The $^5D_0$ decay curve detected at 595.5 nm and excited at 394 nm is well fitted by a biexponential function yielding lifetimes of ca. 2.02 $\pm$ 0.02 and 0.58 $\pm$ 0.02 ms. When compared with the curve measured at 595.5 nm, the contribution of the shorter lifetime to the $^5D_0$ decays decreases for detection within the $^5D_0 \rightarrow ^7F_0$ (579.3 nm) and $^5D_0 \rightarrow ^7F_2$ transitions (610.5 nm). Thus, the longer lifetime is assigned to the Eu^{3+} located in the K(2) position, while the shorter lifetime is attributed to the Eu^{3+} local site in the layers. Moreover, lifetime measurements of $K_3[Y_{1-a}Eu_aSi_3O_8(OH)_2]$ (a = 0.1, 0.2, 0.4, and 0.5) samples indicate that the Eu^{3+} local site in the layers (short lifetime) is present only for $a > 0.2$. Indeed, the decay curves of $a = 0.1$ and 0.2 samples are well fitted by an exponential, yielding lifetimes of ca. 2.46 $\pm$ 0.01 and 2.41 $\pm$ 0.01 ms, respectively. The longer lifetimes of samples $a = 0.4$ and 0.5 are 2.36 $\pm$ 0.01 and 2.32 $\pm$ 0.01 ms, respectively. Hence, the $^5D_0$ lifetime decreases about 17%. Although the concentration quenching effects are more important than observed for $K_3[Y_{1-a}Tb_aSi_3O_8(OH)_2]$ samples, the energy migration between Eu^{3+} ions still play a minor role. The structural similarity of Eu-AV-22 and Tb-AV-22 implies that energy transfer between active optical Eu^{3+} centers located in the layers is unlikely. Thus, the energy migration should occur between Eu^{3+} centers in the layers and in the interlayer space in K(2) positions (probably by both exchange and multipolar interaction mechanisms).

The excitation spectra of $K_3[Tb_{0.95}Eu_{0.05}Si_3O_8(OH)_2]$ and $K_3[EuSi_3O_8(OH)_2]$, monitored at the main $^5D_0 \rightarrow ^7F_2$ line (610.5 nm), display the same Eu^{3+} lines (Figure 10) and, in addition, the characteristic excitation spectrum of $K_3[TbSi_3O_8(OH)_2]$ (Figure 8). This is clear evidence for efficient Tb^{3+}-to-Eu^{3+} energy transfer. Furthermore, the Tb^{3+}-to-Eu^{3+} energy transfer is also detected in the emission of the $K_3[Tb_{0.95}Eu_{0.05}Si_3O_8(OH)_2]$ samples (Figure 11).

The emission spectrum of $K_3[Tb_{0.95}Eu_{0.05}Si_3O_8(OH)_2]$ excited in the Tb^{3+} (377 nm) levels shows the typical Eu^{3+} lines (present in the spectrum of the pure Eu^{3+} sample) and $^5D_4 \rightarrow ^7F_{5,6}$ transitions of the Tb^{3+} pure sample. Similar spectra were recorded with excitation within other Tb^{3+} levels (485 nm, $^5D_4$ and 280 nm, HS fd), not overlapping with Eu^{3+} states. For a sample with higher ($a = 0.1$) Eu^{3+} content, the intensity of the $^5D_4 \rightarrow ^7F_{5,6}$ Tb^{3+} transitions decreases 40%, relative to the sample with $a = 0.05$. This further supports the above-mentioned energy transfer between Tb^{3+} and Eu^{3+}.

Lifetime measurements of these samples (Figure 12) show the presence of two local Eu^{3+} (Tb^{3+}) environments in the mixed Tb^{3+}/Eu^{3+} AV-22 samples. For times up to ca. 4 ms, the $K_3[Tb_{0.95}Eu_{0.05}Si_3O_8(OH)_2]$ decay curve, excited at 377 nm and detected at 610.5 nm, exhibits a nonexponential behavior. Subtracting the $^5D_0$ single-exponential component (lifetime of ca. 2.56 $\pm$ 0.01 ms) from the measured intensity in the time range 0−4 ms, a "grow-in" behavior is observed (inset in Figure 12), which indicates that the decay curves have a contribution from a Tb^{3+}-to-Eu^{3+} energy transfer pathway. Moreover, the Tb^{3+} $^5D_4$ decay curve of $K_3[Tb_{0.95}Eu_{0.05}Si_3O_8(OH)_2]$ (Figure 12) is well fitted by a biexponential function, giving lifetimes of ca. 1.19 $\pm$ 0.02 and 0.68 $\pm$ 0.02 ms. For a sample with higher ($a = 0.1$) Eu^{3+} content, the two Tb^{3+} lifetimes decrease from these values to 0.70 $\pm$ 0.02 and 0.40 $\pm$ 0.02 ms, respectively, due to Tb^{3+}-to-Eu^{3+} energy transfer. A simple operational definition of Tb^{3+}-to-Eu^{3+} energy transfer probability in terms of lifetimes is $P_{Tb\rightarrow Eu} = (1/\tau) - (1/\tau_0)$, where τ and τ_0 are the Tb^{3+} donor lifetimes in the presence and absence of the Eu^{3+} acceptor, respectively.[31,33,35] For the longer lifetime, the values of P are 0.62 ($a = 0.05$) and 1.20 ms^{-1} ($a = 0.1$). The corresponding energy transfer efficiency, $E_{Tb\rightarrow Eu} = (1 - \tau/\tau_0)$,[31,33,35] for these samples is very high, 0.73 and 0.84, respectively.

Efficient Gd^{3+}-to-Tb^{3+} and Tb^{3+}-to-Eu^{3+} energy transfer is also observed in the excitation and emission spectra of AV-22 samples containing a third type of Ln^{3+} ion. This effect clearly shows the remarkable ability to tune the AV-22 system and is illustrated here with the sample $K_3[Gd_{0.67}Tb_{0.28}Eu_{0.05}Si_3O_8(OH)_2]$ (Figure 13).

The XRD structure of AV-22 materials calls for the presence of a single Ln^{3+} environment, while PL spectroscopy shows the presence of two Eu^{3+} and Tb^{3+} sites in $K_3[EuSi_3O_8(OH)_2]$, $K_3[Y_{1-a}Eu_aSi_3O_8(OH)_2]$ ($a \geq 0.5$), and $K_3[Tb_{1-a}Eu_aSi_3O_8(OH)_2]$,

(34) Carlos, L. D.; Videira, A. L. L. *Phys. Rev. B* **1994**, *49*, 11721−11728.

(35) Sendor, D.; Hilder, M.; Juestel, T.; Junk, P. C.; Kynast, U. H. *New J. Chem.* **2003**, *27*, 1070−1077.

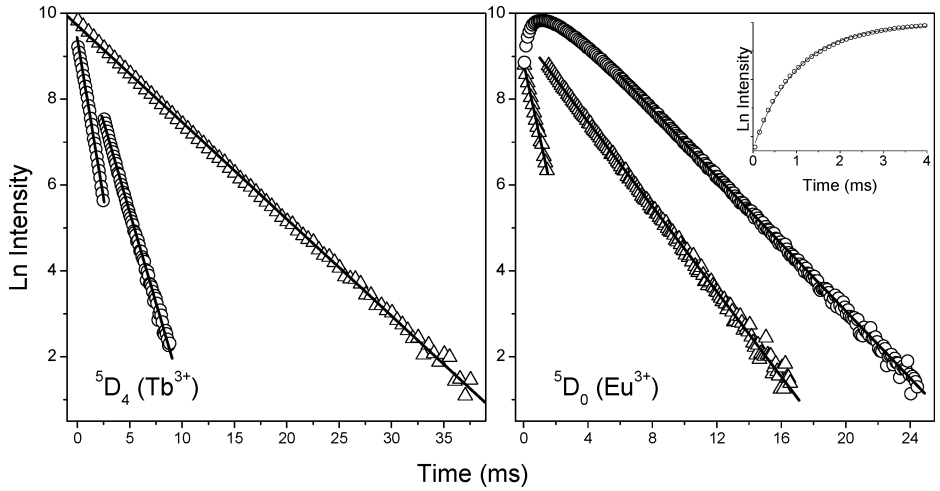

Figure 12. Room-temperature $^5D_0$ and $^5D_4$ decay curves of $K_3[LnSi_3O_8(OH)_2]$ (Ln = Eu^{3+} and Tb^{3+}) (triangles) and $K_3[Tb_{0.95}Eu_{0.05}Si_3O_8(OH)_2]$ (circles) detected at 610.5 (Eu^{3+}) and 541.5 nm (Tb^{3+}). Tb^{3+} was excited at 377 nm (both samples) while Eu^{3+} was excited at 394 and 377 nm for, respectively, $K_3[EuSi_3O_8(OH)_2]$ and $K_3[Tb_{0.95}Eu_{0.05}Si_3O_8(OH)_2]$. The straight lines are the best fits ($r^2 = 0.99$) to the data considering single-exponential and biexponential behavior, respectively. The inset shows the "grow-in" component of the $K_3[Tb_{0.95}Eu_{0.05}Si_3O_8(OH)_2]$ luminescence emission profile. The solid line is a fit to the data ($r^2 = 0.99$) considering an exponential growth function.

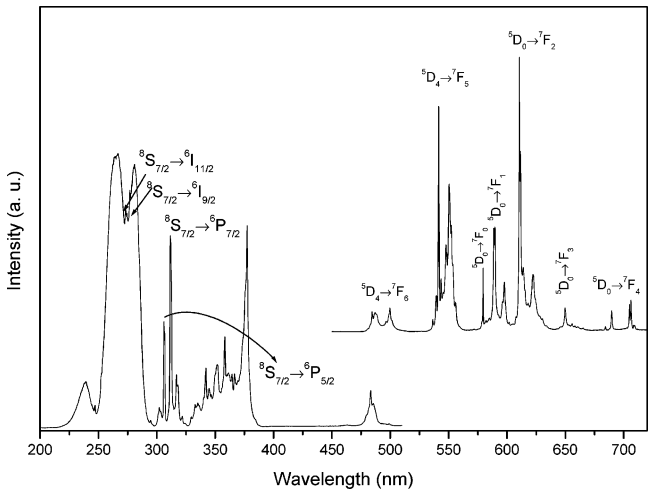

Figure 13. Room-temperature excitation and emission spectra of $K_3[Gd_{0.67}Tb_{0.28}Eu_{0.05}Si_3O_8(OH)_2]$. The excitation was performed at 377 nm, while emission was monitored at 541.5 nm (Tb^{3+} levels). An analogous emission spectrum is obtained for excitation within the $^6P_{7/2,5/2}$ Gd levels.

respectively. PL data indicate that the Ln^{3+} ion may reside in the layers or in the interlayer space. To further investigate this possibility, the crystal structures of $K_3[TbSi_3O_8(OH)_2]$ and the mixed sample $K_3[Tb_{0.9}Eu_{0.1}Si_3O_8(OH)_2]$ were reassessed, but no clear evidence for the presence of interlayer Tb^{3+} (or Eu^{3+}) ions was found. Moreover, the figures of merit of the powder XRD Rietveld refinement of $K_3[EuSi_3O_8(OH)_2]$ did not improve when some Eu^{3+} replaced K^+ ions. We must conclude that photoluminescence is a particularly well-suited technique to detect the presence of relatively small amounts of Eu^{3+} in the interlayer space.

Although it was not possible to calculate exactly the Tb···Eu distances by XRD analysis, indicative values may be obtained from the XRD data of pure Tb-AV-22: Tb···Tb and Tb···K(2) distances are, respectively, ca. 5.9 and 3.8 Å. Thus, Tb^{3+}-to-Eu^{3+} energy transfer is likely to occur (both via exchange and multipolar, dipole−dipole, interactions) between optical centers in the layers and in the interlayer space [K(2) site]. Energy transfer between Tb^{3+} and Eu^{3+} ions present in the layers is unlikely, namely because (i) in $K_3[Y_{1-a}Eu_aSi_3O_8(OH)_2]$ with low Eu content ($a \leq 0.2$) the Eu^{3+} ions are located essentially in the interlayer and (ii) the Tb···Eu estimated distance, ca. 5.9 Å, is comparatively large. In addition, Tb^{3+}-to-Eu^{3+} energy transfer between optical centers in the interlayer space is also unlikely because the few Ln^{3+} ions present will be far apart.

In conclusion, the layered lanthanide silicate system $K_3[M_{1-a}Ln_aSi_3O_8(OH)_2]$ exhibits remarkable photoluminescence properties which may be tuned by judicious choice of the Ln^{3+} ions and the occupancy of the layer and interlayer metal sites. This has been illustrated for M = Y^{3+} and Tb^{3+}, Ln = Eu^{3+}, Er^{3+}, Tb^{3+}, and Gd^{3+}, and it may now be extended to other lanthanide ions.

Acknowledgment. We thank FCT, POCTI, FEDER, and INTERREG IIIB for financial support.

Supporting Information Available: X-ray crystallographic factors, in CIF format. This material is available free of charge via the Internet at http://pubs.acs.org. Further information (excluding structure factors) can be obtained free of charge from Fachinformationszentrum Karlsruhe, 76344, Eggenstein-Leopoldshafen, Germany (e-mail: crysdata@fiz-karlsruhe.de), on quoting the depository numbers CSD-413425 (Tb-AV-22), CSD-413883 (Eu-AV-22), and CSD-413884 (Er-AV-22).

JA047905N